KeAi

CHINESE ROOTS
GLOBAL IMPACT

Contents lists available at ScienceDirect

Petroleum Science

journal homepage: www.keaipublishing.com/en/journals/petroleum-science



Original Paper

Full waveform inversion with fractional anisotropic total p-variation regularization



Bo Li ^{a, b, c}, Xiao-Tao Wen ^{b, c, *}, Yu-Qiang Zhang ^{b, c}, Zi-Yu Qin ^d, Zhi-Di An ^{b, c}

- a Geophysics Postdoctoral Research Station, College of Geophysics, Chengdu University of Technology, Chengdu, 610059, Sichuan, China
- ^b College of Geophysics, Chengdu University of Technology, Chengdu, 610059, Sichuan, China
- ^c Key Laboratory of Earth Exploration and Information Techniques, Ministry of Education, Chengdu University of Technology, Chengdu, 610059, Sichuan, China
- ^d School of Computer Engineering, Chengdu Institute of Technology, Chengdu, 610031, Sichuan, China

ARTICLE INFO

Article history: Received 18 April 2024 Received in revised form 28 January 2025 Accepted 9 May 2025 Available online 10 May 2025

Edited by Meng-Jiao Zhou

Keywords: Full waveform inversion Anisotropic total p-variation Fractional-order differences Sparse regularization

ABSTRACT

Full waveform inversion is a precise method for parameter inversion, harnessing the complete wavefield information of seismic waves. It holds the potential to intricately characterize the detailed features of the model with high accuracy. However, due to inaccurate initial models, the absence of low-frequency data, and incomplete observational data, full waveform inversion (FWI) exhibits pronounced nonlinear characteristics. When the strata are buried deep, the inversion capability of this method is constrained. To enhance the accuracy and precision of FWI, this paper introduces a novel approach to address the aforementioned challenges-namely, a fractional-order anisotropic total p-variation regularization for full waveform inversion (FATpV-FWI). This method incorporates fractional-order total variation (TV) regularization to construct the inversion objective function, building upon TV regularization, and subsequently employs the alternating direction multiplier method for solving. This approach mitigates the step effect stemming from total variation in seismic inversion, thereby facilitating the reconstruction of sharp interfaces of geophysical parameters while smoothing background variations. Simultaneously, replacing integer-order differences with fractional-order differences bolsters the correlation among seismic data and diminishes the scattering effect caused by integer-order differences in seismic inversion. The outcomes of model tests validate the efficacy of this method, highlighting its ability to enhance the overall accuracy of the inversion process.

© 2025 The Authors. Publishing services by Elsevier B.V. on behalf of KeAi Communications Co. Ltd. This is an open access article under the CC BY-NC-ND license (http://creativecommons.org/licenses/by-nc-nd/4.0/).

1. Introduction

Full waveform inversion calculates the gradient by subtracting theoretical seismic data from real data, and subsequently updates inversion parameters (Tarantola, 1984; Mora, 1987; Plessix, 2006, 2009; Qu et al., 2020; Li and Qu, 2022; Barnier et al., 2023; Li et al., 2024). Nonetheless, FWI is a strongly nonlinear and ill-posed inverse problem, making it prone to periodic jumps, making it susceptible to cycle skipping. Particularly when a substantial gap exists between the initial model and the real model, the convergence of the objective function tends to be sluggish, demanding significant time costs and carrying the risk of easily converging into local extreme values. A viable approach to mitigate this issue is by employing objective functions with more convex characteristics.

While previous methods have introduced various objective functions to address these challenges, practical implementations are still influenced by factors such as data complexity and computational costs (Warner and Guasch, 2016; Yao et al., 2020).

To address such challenges, regularization methods can be incorporated to prevent overfitting or ill-posedness of the data. In this context, traditional FWI employs the L_2 norm as the objective function, utilizes the adjoint state method for gradient calculation, and iteratively updates the model parameters of the subsurface medium in the direction of gradient descent. The regularization result with L_2 norm tends to be smoother. In cases where the initial model is inadequate, there is a lack of long-offset transmission data, or the data includes a certain level of noise, the inversion outcome may be suboptimal. In contrast, utilizing L_1 norm constraints in the inversion process yields superior results (Burstedde and Ghattas, 2009; Brossier et al., 2009, 2010; Virieux and Operto, 2009; Guitton, 2012; Aghamiry et al., 2018).

E-mail address: wenxiaotao@cdut.edu.cn (X.-T. Wen).

^{*} Corresponding author.

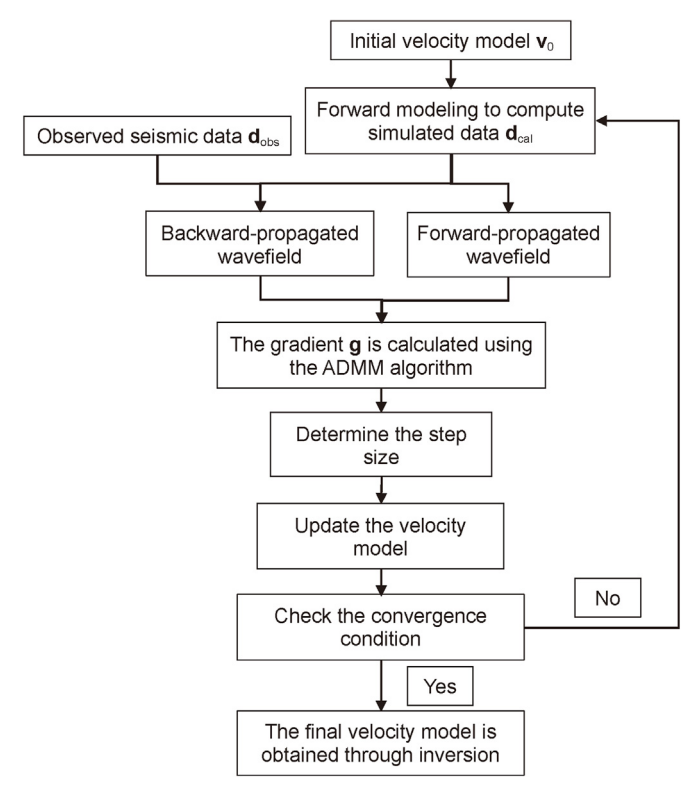


Fig. 1. Flow chart.

Introducing constraint methods can improve the accuracy of FWI (Lin and Huang, 2014; Li et al., 2016; Guo et al., 2020; Zhu et al., 2017; Li et al., 2023; Zhu et al., 2022). Yu et al. (2014) proposed a mixed dual-parameter regularization approach that combines the L_2 norm with the non-smooth L_1 norm. This method exhibits rapid convergence towards the true model and demonstrates high inversion accuracy. The total variation regularization constraint term is one of the commonly used sparse forms in compressive sensing, capable of simultaneously constraining both horizontal and vertical differences. Compared to the L_1 norm sparse constraint, it can introduce more available information. Esser et al. (2018) formulated the TV regularized objective function for full waveform inversion (TV-FWI), highlighting its capability to

enhance inversion quality across diverse initial models. Yong et al. (2018) introduced an adaptive primitive-dual mixed gradient method which achieves TV regularization by projecting solutions onto a convex set constrained by the total variation norm. This ensures adherence to total variation norms at each iteration. thereby enhancing the accuracy of FWI. Aghamiry et al. (2019b) enhanced the accuracy of FWI by devising hybrid regularization methods incorporating Tikhonov and total variation functionals. These hybrid regularizers offer improved flexibility in handling diverse inversion scenarios. Kalita et al. (2019) addressed challenges associated with salt-affected datasets in FWI by integrating model regularization techniques. This approach enables the representation of large high-velocity structures over wide regions, surpassing the limitations of conventional FWI. Zhang et al. (2022) introduced a weak total variation constraint in FWI to mitigate over-smoothing issues arising from strong total variation constraints. This refinement allows for a more accurate estimation of the model. In order to improve the quality of FWI results, many researchers have improved regularization methods to constrain the objective function (Esser et al., 2018; Aghamiry et al., 2019a; Xue et al., 2017; Gupta et al., 2018; Qu et al., 2019).

The horizontal and vertical differences of TV regularization mentioned above share the same properties, hence they are referred to as isotropic total variation (ITV). Besides ITV regularization, there exists another form of total variation with distinct properties in different directions, known as anisotropic total variation (ATV). Although ATV regularization incorporates more sparse information, the L₁ norm employed in ATV regularization is not the optimal method for representing sparsity. Compared to the L₁ norm, the L_p pseudo-norm exhibits superior sparsity. Consequently, an anisotropic total variation based on L_n-norm (ATpV) constraint term has emerged. ATpV regularization excels in enhancing the texture of smooth areas, preserving information, and mitigating large oscillations in edge regions. This characteristic aids in reducing scattering effects, ultimately enhancing inversion accuracy (Woodworth and Chartrand, 2016). In contrast to integer differencing, fractional differencing extends its reach by amplifying texture information in smooth regions, while sidestepping pronounced edge oscillations, thus minimizing scattering effects (Bai and Feng, 2007). Didas et al. (2005) theoretically proved that fractional-order differencing achieves greater variance reduction compared to integer-order differencing, and this was corroborated through image restoration, yielding superior outcomes. Zhang et al.

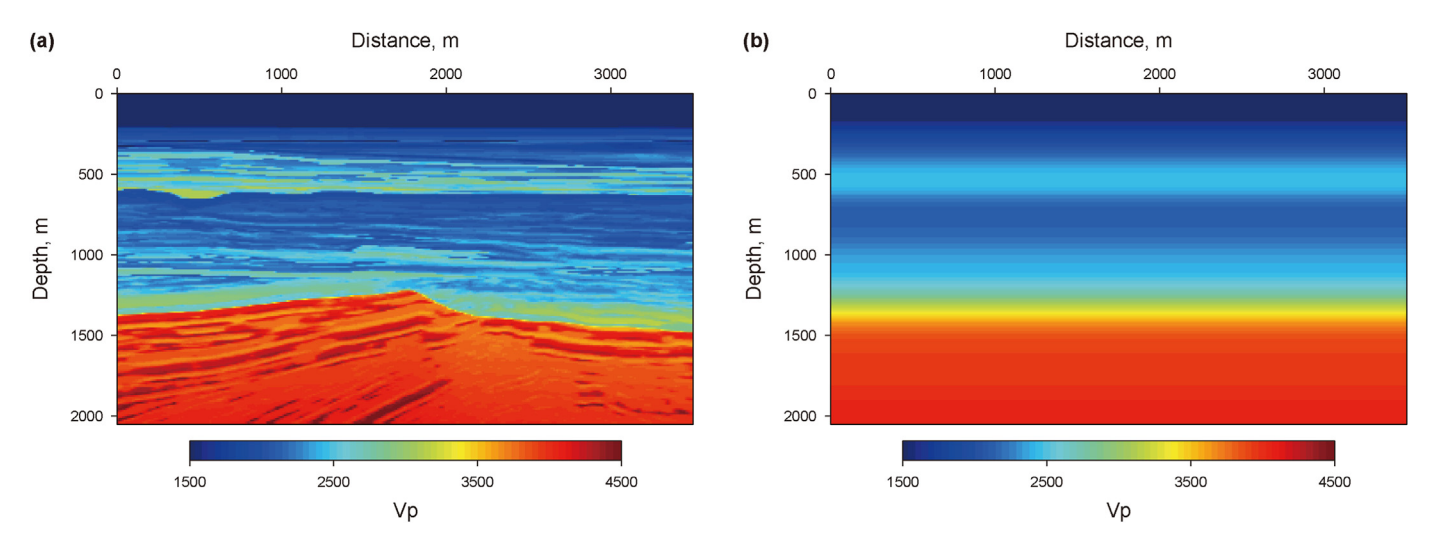


Fig. 2. The theoretical model. (a) Velocity model; (b) initial velocity model.

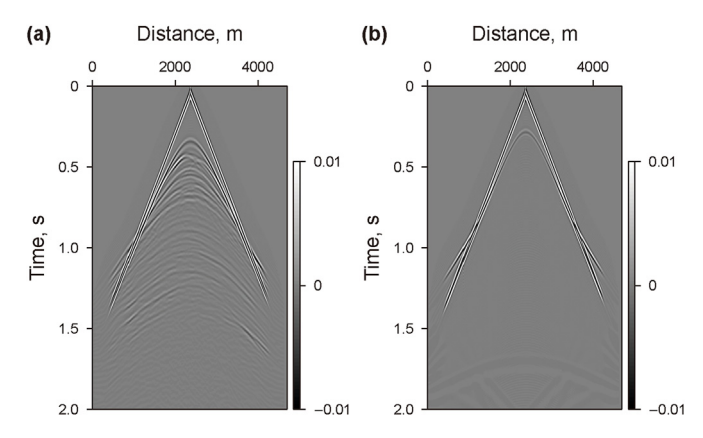


Fig. 3. Single-shot gather. **(a)** Single-shot gather obtained by the true velocity model; **(b)** single-shot gather obtained by the initial velocity model.

(2012) implemented fractional-order differencing in image restoration, revealing that fractional-order anisotropic regularization (FATV) can mitigate scattering effects. Meanwhile, research has demonstrated that the anisotropic total L_p variation regularization

constraint based on the L_p pseudo norm (0 < p < 1) (FATpV), exhibits higher image accuracy compared to traditional FATV restoration (Li et al., 2018a, 2018b; Wu et al., 2019; Chen et al., 2020).

Hence, building upon the aforementioned theory, this paper suggests a fractional-order anisotropic total variation regularization method based on L_p quasi-norm for implementation in FWI. The paper initially outlines the solution process of FWI and subsequently elaborates on the derivation of the objective function and the solution process for fractional-order anisotropic total variation regularization based on L_p quasi-norm. The Alternating Direction Method of Multipliers (ADMM, Boyd et al., 2011) algorithm is employed to address the problem, ultimately leading to the inversion and acquisition of seismic velocity. The validity of this method is confirmed through two model tests.

2. Theory and methodology

FWI is a technique employed in seismic imaging and the reconstruction of subsurface media models. It entails generating a high-resolution model of the underground medium by comparing observed seismic waveforms with numerically simulated seismic waveforms. This process can be expressed as:

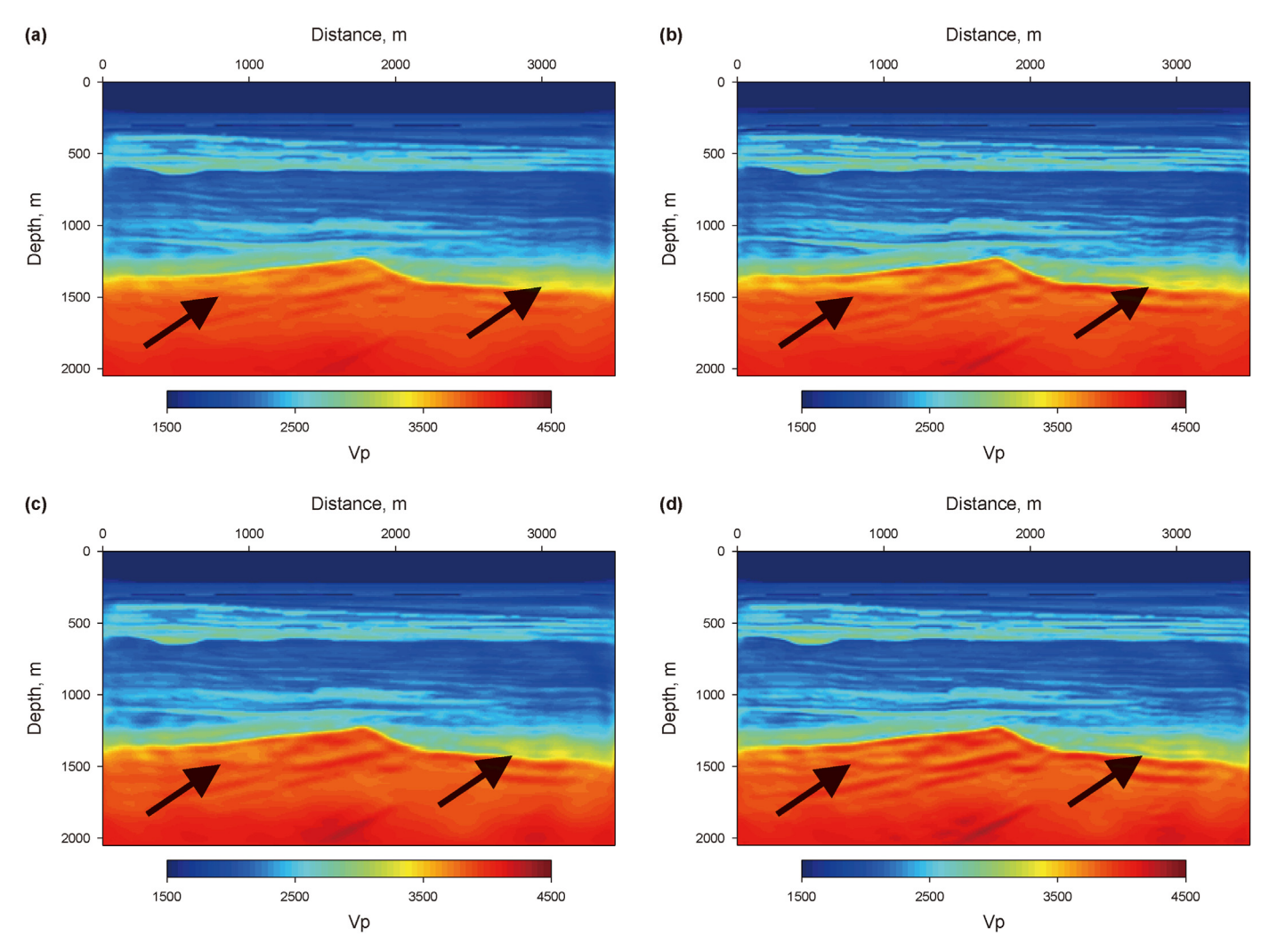


Fig. 4. FWI example: inverted velocity using (a) regular FWI without any regularization, (b)TV-FWI, (c) ATpV-FWI, and (d) FATpV-FWI.

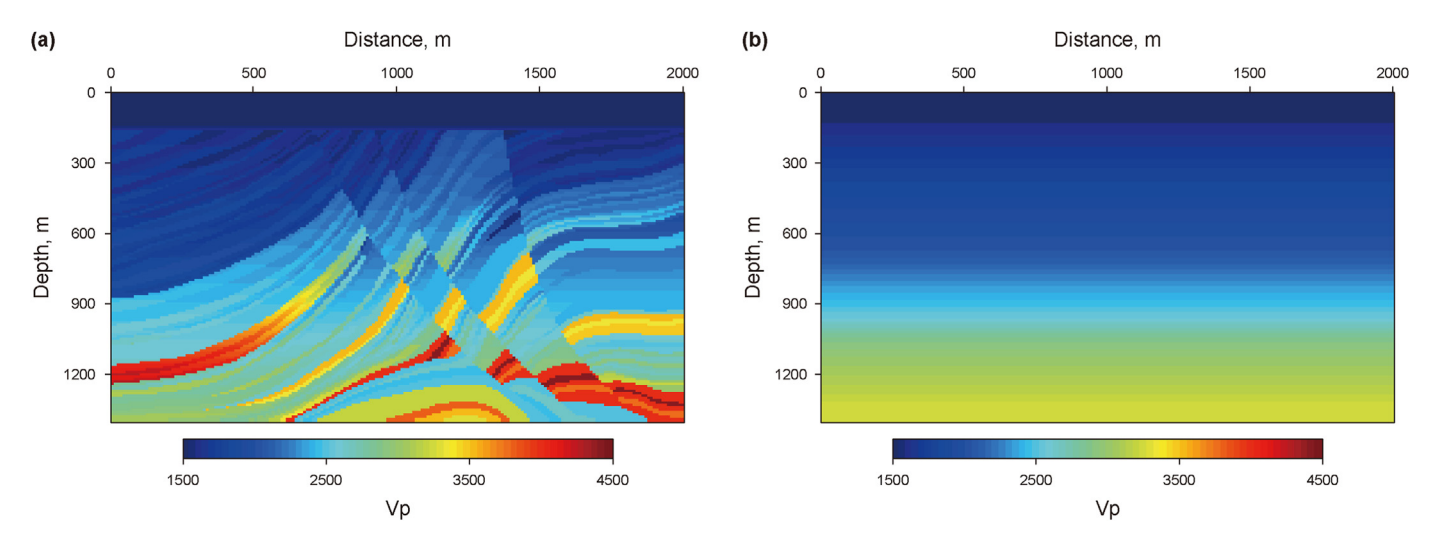


Fig. 5. The theoretical model. (a) Velocity model; (b) initial velocity model.

$$E(\mathbf{m}) = \min_{\mathbf{m}} \left\{ \frac{1}{2} \|\mathbf{d}_{\text{obs}} - \mathbf{d}_{\text{cal}}(\mathbf{m})\|_{2}^{2} \right\}, \tag{1}$$

where $E(\mathbf{m})$ represents the objective function, \mathbf{m} signifies the underground medium model, \mathbf{d}_{obs} corresponds to the real seismic data, and \mathbf{d}_{cal} denotes the data acquired through forward modeling.

Currently, TV regularization is extensively applied in the realm of seismic exploration. It offers the benefits of preserving data details and edge features, noise suppression, enhanced robustness, and the promotion of sparsity. Therefore, the minimization problem defining total variation regularization is as follows:

$$E(\mathbf{m}) = \min_{\mathbf{m}} \left\{ \frac{1}{2} \|\mathbf{d}_{\text{obs}} - \mathbf{d}_{\text{cal}}(\mathbf{m})\|_{2}^{2} + \lambda \|\nabla \mathbf{m}\|_{1} \right\}, \tag{2}$$

where λ is a regularization parameter, $\|\nabla \mathbf{m}\|_1$ is a discrete operator, which means seeking partial derivatives in the x and z directions. Let $\varphi_1(\mathbf{m}) = \|\nabla \mathbf{m}\|_1$, then $\varphi_1(\mathbf{m})$ can be expressed as:

$$\varphi_1(\mathbf{m}) = \sum_{i,j} \sqrt{(\nabla_x \mathbf{m})_{i,j}^2 + (\nabla_y \mathbf{m})_{i,j}^2} = \|\mathbf{m} \mathbf{D}_x\|_1 + \|\mathbf{D}_y \mathbf{m}\|_1,$$
 (3)

where \mathbf{D}_x represents the horizontal difference, \mathbf{D}_y represents the vertical difference. If it is ATpV regularization, \mathbf{D}_x and \mathbf{D}_y should be expressed as:

$$\mathbf{D}_{X} = \begin{bmatrix} -1 & 0 & \cdots & 0 & 1 \\ 1 & -1 & \ddots & \vdots & 0 \\ 0 & 1 & \ddots & \vdots & \vdots \\ \vdots & \ddots & \ddots & -1 & 0 \\ 0 & 0 & \cdots & 1 & -1 \end{bmatrix}_{N_{y} \times N_{y}}, \mathbf{D}_{y} = \begin{bmatrix} -1 & 1 & 0 & \cdots & 0 \\ 0 & -1 & 1 & \ddots & \vdots \\ \vdots & \ddots & \ddots & \ddots & 0 \\ 0 & \cdots & \cdots & -1 & 1 \\ 1 & 0 & \cdots & 0 & -1 \end{bmatrix}_{N_{x} \times N_{y}}$$

$$(4)$$

Nevertheless, employing first-order total variation as the regularization constraint for the solution tends to introduce imperfect sparse information and can readily induce a staircase effect (Wu et al., 2019). Building upon this foundation, we integrate L_p quasinorm with anisotropic total variation difference to formulate an anisotropic total variation difference based on L_p quasi-norm constraint. Its objective function is:

$$E(\mathbf{m}) = \min_{\mathbf{m}} \left\{ \frac{1}{2} \|\mathbf{d}_{\text{obs}} - \mathbf{d}_{\text{cal}}(\mathbf{m})\|_{2}^{2} + \lambda \varphi_{2}(\mathbf{m}) \right\}, \tag{5}$$

where $\varphi_2(\mathbf{m}) = (\|\mathbf{m}\mathbf{D}_x^a\|_p^p + \|\mathbf{D}_y^a\mathbf{m}\|_p^p)$, the fractional difference is expressed as:

$$\mathbf{D}_{y}^{a}\mathbf{m}(i,j) = \sum_{i=0}^{k} \psi_{a}(l)\mathbf{m}(i-1,j)$$
(6)

where i and j represent the positions in the vertical and horizontal directions respectively, a is a fraction, which determines the size of the fractional factorial, and k is an integer, which determines the number of differences of the parameters to be inverted. And $\psi_a(l)$ is defined as follows:

$$\psi_a(l) = (-1)^l \Gamma(a+1) / [(l!)\Gamma(a-l+1)], \tag{7}$$

where $\Gamma(a) = \int_0^{+\infty} t^{a-1} e^{-t} dt$, $l! = 1 \times 2 \times \cdots \times l$, so the fractional-order longitudinal difference $\mathbf{D}_{\mathbf{v}}^a$ and $\mathbf{D}_{\mathbf{x}}^a$ should be expressed as:

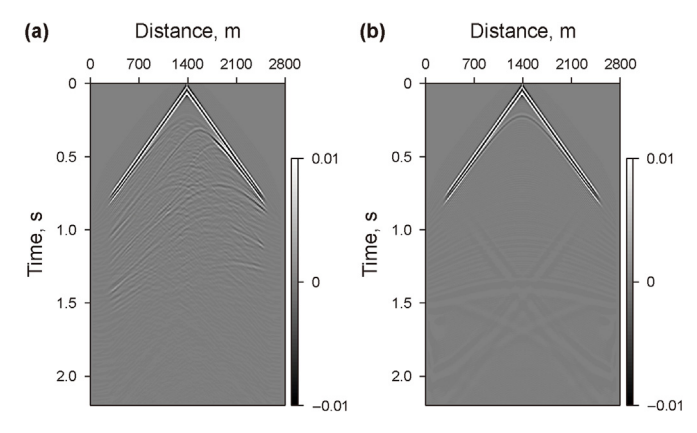


Fig. 6. Single-shot gather. **(a)** Single-shot gather obtained by the true velocity model; **(b)** single-shot gather obtained by the initial velocity model.

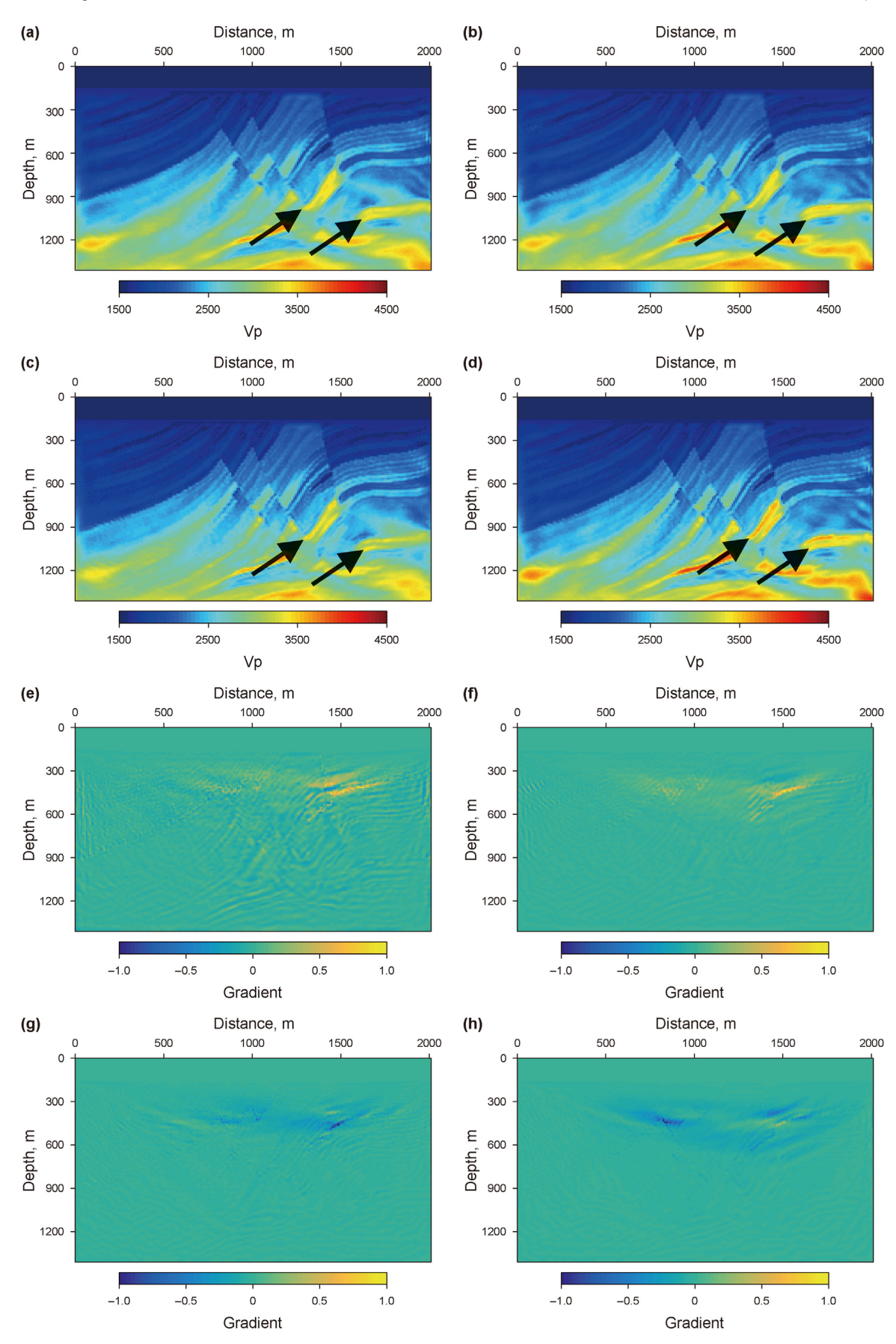


Fig. 7. FWI example: inverted velocity using (a) regular FWI without any regularization, (b) TV-FWI, (c) ATpV-FWI and (d) FATpV-FWI. Velocity gradient from the residual at the final iteration using (e) regular FWI without any regularization, (f) TV-FWI, (g) ATpV-FWI and (h) FATpV-FWI.

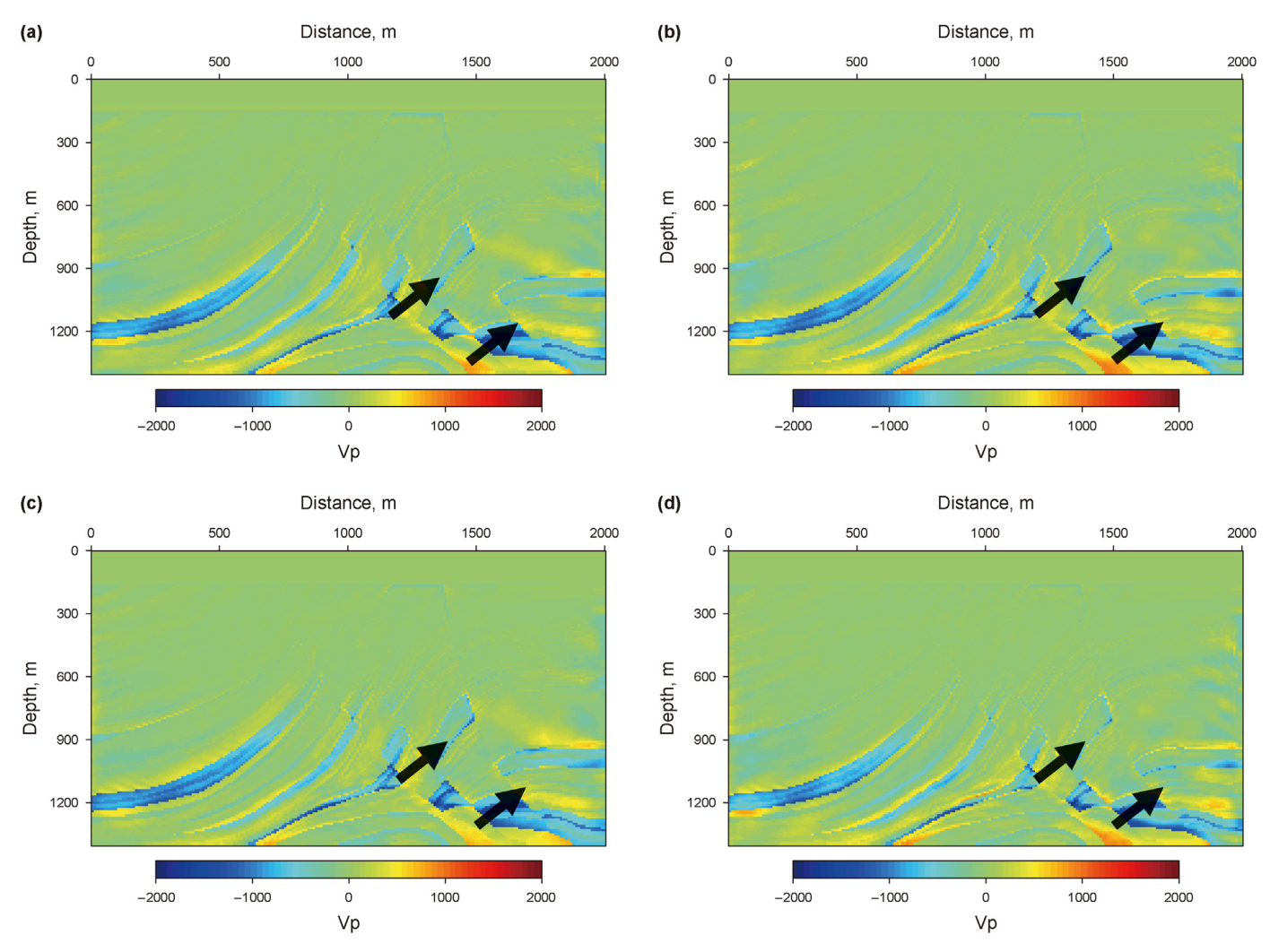


Fig. 8. (a)-(d) The difference between real Vp and the inverted by regular FWI without any regularization, TV-FWI, ATpV-FWI, and FATpV-FWI.

$$\mathbf{D}_{y}^{a} = \begin{bmatrix} \psi_{a}(k) & \cdots & \psi_{a}(1) & \psi_{a}(0) & 0 & \cdots & 0 \\ 0 & \ddots & \vdots & \psi_{a}(1) & \psi_{a}(0) & \ddots & \vdots \\ \vdots & \ddots & \psi_{a}(k) & \vdots & \psi_{a}(1) & \ddots & 0 \\ 0 & \vdots & 0 & \psi_{a}(k) & \vdots & \ddots & \psi_{a}(0) \\ \psi_{a}(0) & \ddots & \vdots & 0 & \psi_{a}(k) & \ddots & \psi_{a}(1) \\ \vdots & \ddots & 0 & \vdots & \ddots & \ddots & \vdots \\ \psi_{a}(k-1) & \cdots & \psi_{a}(0) & 0 & \cdots & 0 & \psi_{a}(k) \end{bmatrix}_{N_{y} \times N_{y}},$$

$$\mathbf{D}_{x}^{a} = \begin{bmatrix} \psi_{a}(k) & 0 & \cdots & 0 & \psi_{a}(0) & \cdots & \psi_{a}(k-1) \\ \vdots & \ddots & \ddots & \cdots & \ddots & \ddots & \vdots \\ \psi_{a}(1) & \cdots & \psi_{a}(k) & 0 & \cdots & 0 & \psi_{a}(0) \\ \psi_{a}(0) & \psi_{a}(1) & \cdots & \psi_{a}(k) & 0 & \cdots & 0 \\ 0 & \psi_{a}(0) & \psi_{a}(1) & \cdots & \psi_{a}(k) & \ddots & \vdots \\ \vdots & \ddots & \ddots & \ddots & \ddots & \ddots & 0 \\ 0 & \cdots & 0 & \psi_{a}(0) & \psi_{a}(1) & \cdots & \psi_{a}(k) \end{bmatrix}_{N_{x} \times N_{x}}$$

$$(8)$$

Putting $\varphi_2(\mathbf{m}) = (\|\mathbf{m} \mathbf{D}_x^a\|_p^p + \|\mathbf{D}_y^a \mathbf{m}\|_p^p)$ into Eq. (5), it can be rewritten as:

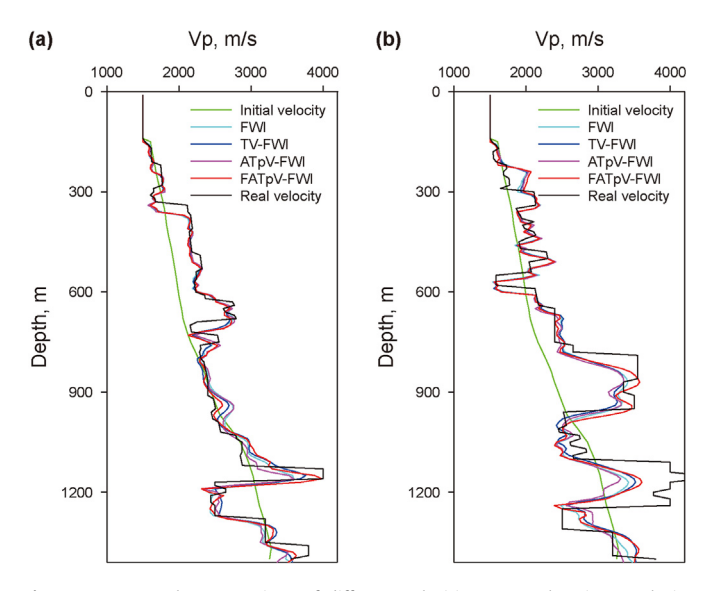


Fig. 9. FWI example: comparison of different velocities at two locations. Velocity comparison at **(a)** x = 1100 m, **(b)** x = 1400 m. (Light green represents the initial velocity, black represents the theoretical velocity, sky blue represents the conventional inversion result, blue represents the TV-FWI inversion result, magenta represents the ATpV-FWI inversion result, and red represents the FATpV-FWI inversion result.)

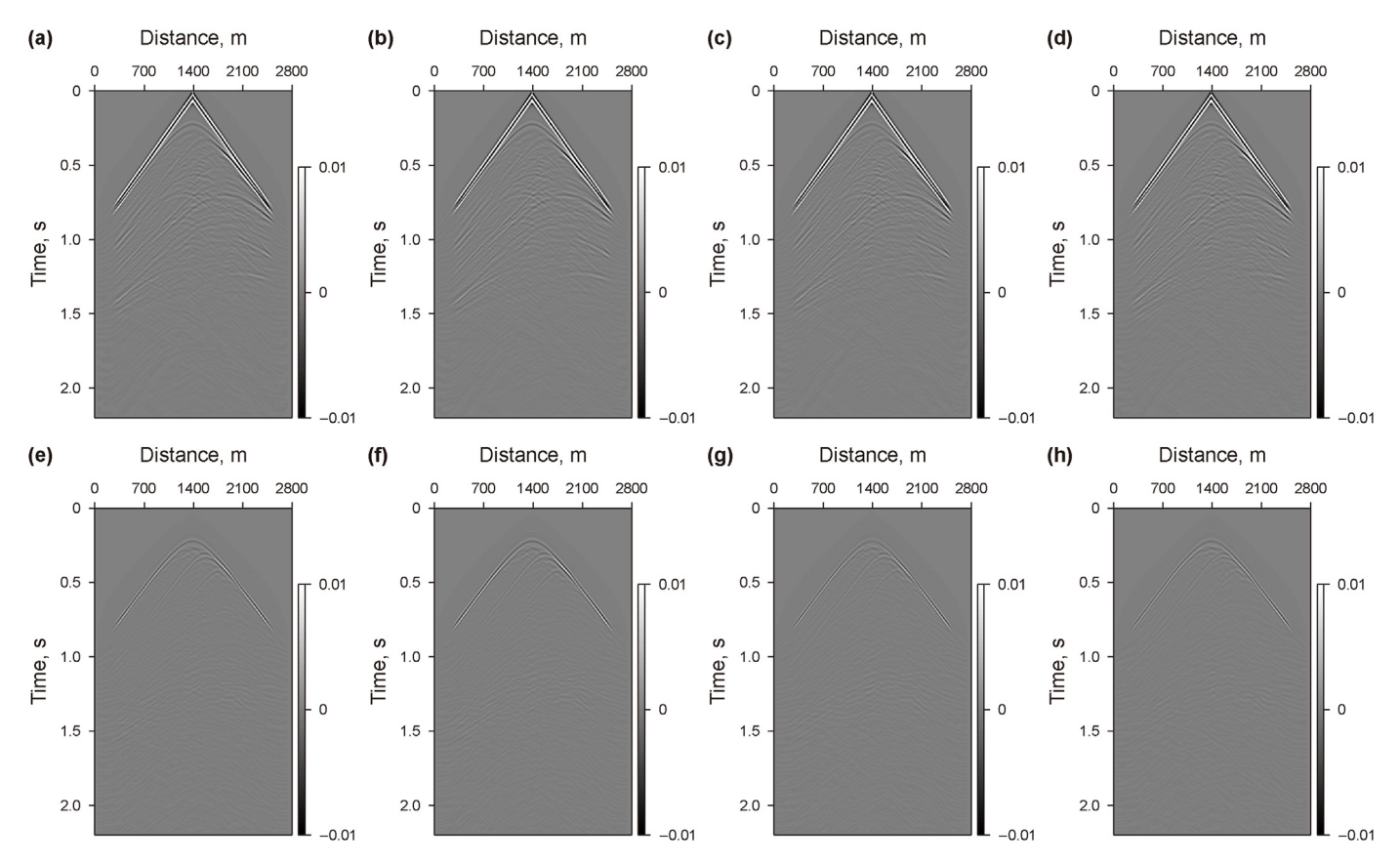


Fig. 10. Single-shot gather. (a)—(d) Single-shot gather by regular FWI without any regularization, TV-FWI, ATpV-FWI and FATpV-FWI. (e)—(h) The difference between real single-shot gather and the single-shot gather by regular FWI without any regularization, TV-FWI, ATpV-FWI, and FATpV-FWI.

$$E(\mathbf{m}) = \min_{\mathbf{m}} \left\{ \frac{1}{2} \|\mathbf{d}_{\text{obs}} - \mathbf{d}_{\text{cal}}(\mathbf{m})\|_{2}^{2} + \lambda \left(\|\mathbf{m} \mathbf{D}_{x}^{a}\|_{p}^{p} + \|\mathbf{D}_{y}^{a} \mathbf{m}\|_{p}^{p} \right) \right\}.$$

$$(9)$$

Using ADMM algorithm, the objective function is decomposed into functions about the sub-functions, and can be obtained by alternately solving. Among them, the sub-functions are expressed as:

$$\begin{cases}
\mathbf{m}_{l+1} = \min_{\mathbf{m}} \left\{ \frac{1}{2} \|\mathbf{d}_{obs} - \mathbf{d}_{cal}(\mathbf{m})\|_{2}^{2} + \frac{\eta}{2} \|\mathbf{m} - \mathbf{w}_{l} + \mathbf{b}_{l}\|_{2}^{2} \right\} \\
\mathbf{w}_{l+1} = \min_{\mathbf{w}} \left\{ \lambda \left(\|\mathbf{m} \mathbf{D}_{x}^{a}\|_{p}^{p} + \|\mathbf{D}_{y}^{a} \mathbf{m}\|_{p}^{p} \right) + \frac{\eta}{2} \|\mathbf{m}_{l+1} - \mathbf{w} + \mathbf{b}_{l}\|_{2}^{2} \right\}, \\
\mathbf{b}_{l+1} = \mathbf{b}_{l} + \mathbf{m}_{l+1} - \mathbf{w}_{l+1}
\end{cases} (10)$$

where **w** and **b** are intermediate variables. Please see Appendix A for the specific derivation and solution process. Under the calculation of the above steps, we can perform parameter inversion, and its flow chart is shown in Fig. 1.

3. Examples

To validate the efficacy of the proposed method in this paper, we employ the BG Compass model for verification. Fig. 2(a) illustrates the theoretical velocity model, while Fig. 2(b) presents the initial velocity model. This model consists of 350×205 grid points with spacing of 10 m in the horizontal and vertical directions. The record length is 2 s at sampling rate of 1 ms, and 35 shots distributed on the surface for excitation. The source is a 20 Hz Ricker wavelet, and

seismometers are uniformly covered at the surface. All the FWI methods compared in the article were calculated using the multiscale method, with frequencies of 3, 6, 10, and 20 Hz, each frequency was iterated 20 times.

Fig. 3(a), (b) depict the comparison of seismic records for the 18th shot in the theoretical model and the initial model, respectively. It is evident from the figures that the seismic waveform obtained through forward modeling in the initial model appears relatively simplistic, lacking the reflection of numerous detailed information. In contrast, single-shot gather of the theoretical model distinctly reveals reflected waves from beneath the stratum. By computing the difference between the theoretical seismic waveform and the waveform obtained in the initial model, underground parameters can be inverted using the formulated equation.

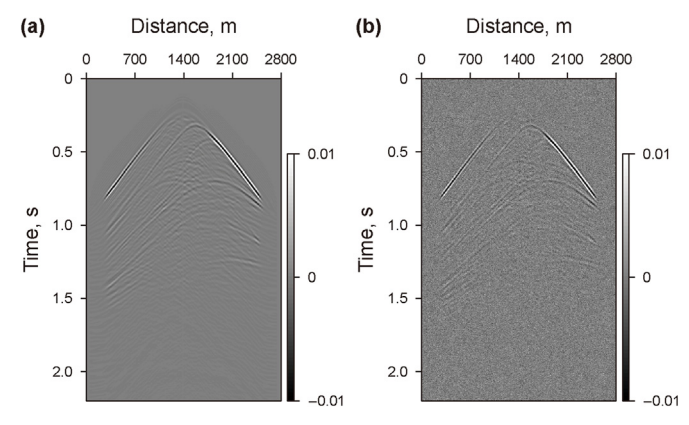


Fig. 11. Clean seismic data (a) and noisy seismic data (b).

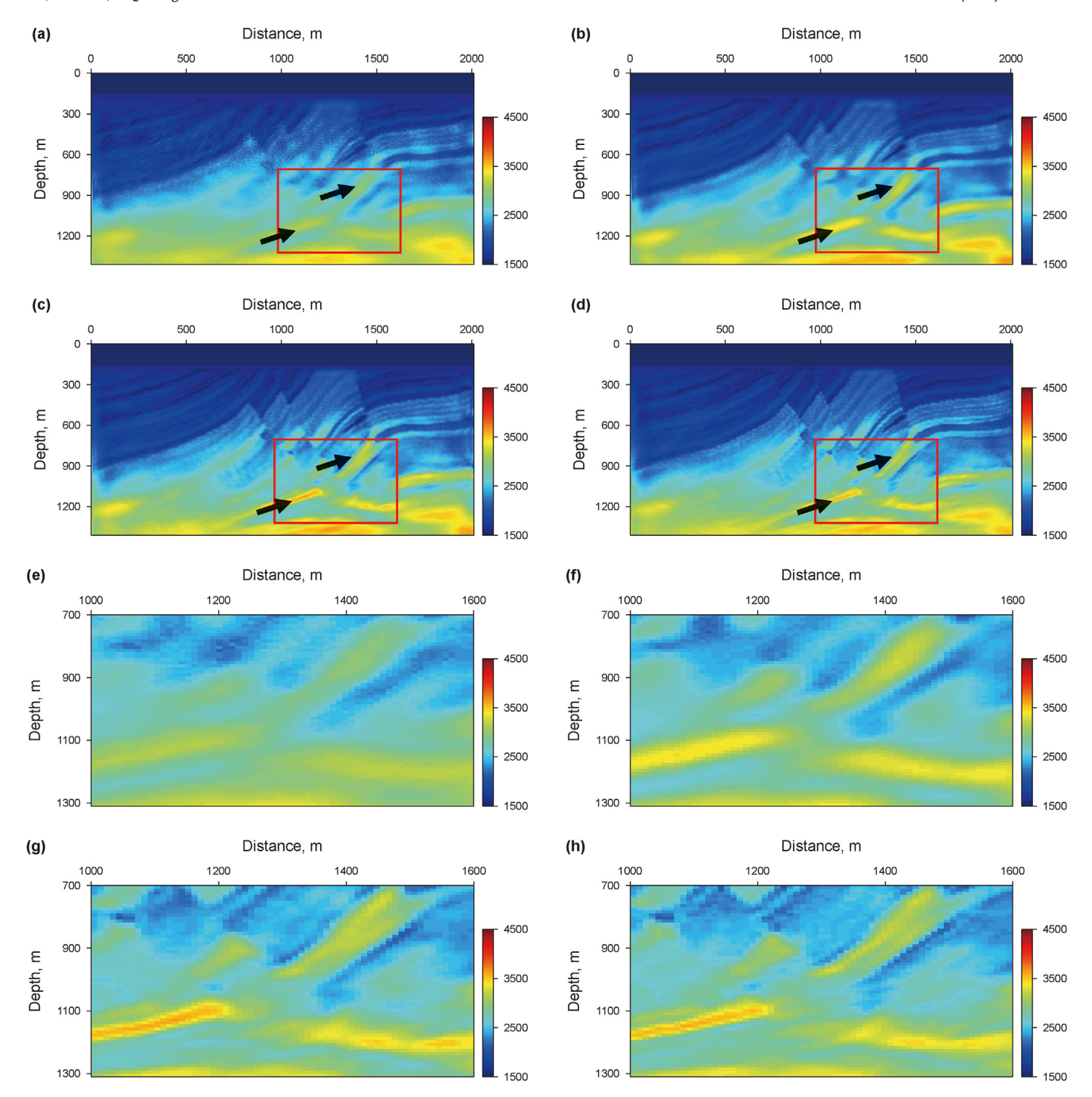


Fig. 12. FWI example: inverted velocity using (a) regular FWI without any regularization, (b) FWI with conventional TV, (c) FWI with ATpV, and (d) FWI with FATpV, (e)—(h) the corresponding partial enlarged pictures respectively.

Fig. 4(a)—(d) display the outcomes of regular FWI without any regularization, TV-FWI regularized inversion, ATpV-FWI and FATpV-FWI, respectively. In comparison with the initial model velocity, all four inversion results exhibit improved resolution to varying degrees. However, notably, it is worth noting that the method proposed in this article is superior to the other three methods in terms of results. For instance, in the deeply embedded high-speed anomaly within the model, the resolution of results obtained by the conventional inversion method is notably low, making it challenging to discern the velocity abnormal area within

the high-speed body. While TV regularization fares better than the conventional method, allowing for the identification of some abnormal areas, Fig. 4(d) clearly illustrates that the velocity recovery achieved by the proposed method surpasses the performance of the other three. The velocity interfaces between adjacent formations are distinct, and the recovered speed values closely align with those of the real model.

To validate the effectiveness of the method proposed in this article, we extracted the Marmousi-2 model from SEG/EAGE and conducted a comparative analysis involving multiple methods. The

geological profile in the model predominantly comprises mudstone layers with a few sandstone layers. The bottom of the intricate fault zone forms an anticline composed of mudstone and limestone, exhibiting significant horizontal and vertical velocity variations in the model. This model is commonly employed for seismic migration imaging and inversion purposes. Fig. 5(a) illustrates the theoretical velocity model, and Fig. 5(b) initial velocity model. The model grid points are configured as $nx \times nz = 200 \times 140$, with a grid interval of $\Delta x = \Delta z = 10$ m, a time step of $\Delta t = 1$ ms, and a total of 20 shots received over 2.2 s. The seismic source utilized is a 20 Hz main frequency Ricker wavelet, with detectors uniformly covering the surface.

Fig. 6(a) and (b) present a comparison of the seismic records for the 10th shot in the theoretical model and the initial model, respectively. It is evident from the figures that the seismic waveforms obtained through forward modeling in the initial model appear relatively straightforward. Simultaneously, waveforms such as seafloor multiples and refraction waves are observable at far offsets. However, the residual difference between the simulated seismic records and the observed seismic records of the initial model highlights the intricacies in the velocity distribution of the Marmousi-2 model, particularly the pronounced changes in lateral velocity.

Fig. 7(a)—(d) illustrate the outcomes of regular FWI without any regularization, TV regularized inversion, ATpV-FWI and the inversion method proposed in this paper, respectively. In comparison with the initial model velocity, all four results exhibit improved resolution to varying degrees. The sequential relationships of the strata and the macrostructure, such as the strike and dip angle of the strata, have been well restored. Notably, the location and shape of faults in the middle of the model have been accurately reproduced. However, in contrast, the traditional method, TV-FWI and ATpV-FWI are surpassed by the method in this paper. For instance, the thickness of the gas-bearing sandstone on the left side of the model appears excessive in the results of the traditional method and TV-FWI, and the direction of the fault plane in the middle, along with the boundary of the formation velocity in the fault body, are less distinct. In contrast, the proposed method excels in

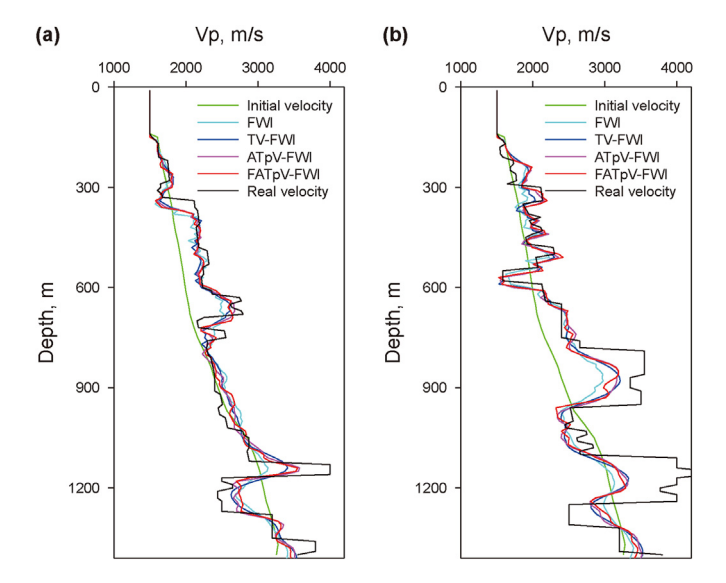


Fig. 13. FWI example: comparison of different velocities at two locations. Velocity comparison at (a) x = 1100 m, (b) x = 1400 m. (Light green represents the initial velocity, black represents the theoretical velocity, sky blue represents the conventional inversion result, blue represents the TV-FWI inversion result, magenta represents the ATpV-FWI inversion result, and red represents the FATpV-FWI inversion result.)

formation velocity recovery. The velocity interfaces between adjacent formations are clear, and the numerical recovery of the formation velocity closely aligns with the velocity of the real model.

Fig. 7(e)—(h) depict the ultimate gradient maps for conventional inversion results, TV regularization inversion results, ATpV-FWI and our inversion results, respectively. It is apparent from the graphs that the final gradient update in the inversion method proposed in this article is more uniform, resulting in a faster update of deep parameters. In contrast, the conventional method and TV regularization inversion method exhibit more concentrated gradients in the shallow layer, proving less effective in inverting deep underground parameters. Fig. 8(a)—(d) represent the difference between real Vp and the inverted by regular FWI without any regulation, TV-FWI, ATpV FWI, and FATpV FWI. As can be seen from the arrows in the figures, the error of our method is smaller.

Fig. 9 shows a single channel comparison of the inversion results in Fig. 7, where light green represents the initial velocity, black represents the theoretical velocity, sky blue represents the conventional inversion result, blue represents the TV-FWI inversion result, magenta represents the ATpV-FWI inversion result, and red represents the method proposed in this paper. From the graph, it can be seen that the red color has the best effect. Fig. 10(a)–(d) present the single-shot gather acquired through conventional inversion, TV regularization inversion, ATpV-FWI and the inversion method proposed in this paper, respectively. Each dataset in the figures differs from the theoretical data, yet they all exhibit striking similarities, making it challenging to discern which method is superior. The disparities between each individual shot dataset and the real data are illustrated in Fig. 10(e)-(h). It is evident from the figures that the single-shot gather obtained through conventional inversion significantly deviate from the theoretical single-shot gather, manifesting a notable error in the record difference. The difference between the single-shot gather obtained through TV regularization inversion and the real single-shot gather exhibits a substantial shallow error. In contrast, the difference between the single-shot gather obtained through the inversion method in this paper and the theoretical single-shot gather demonstrates the smallest error. This further underscores the effectiveness of the proposed method.

Given the inevitability of noise in field seismic data, we introduced Gaussian white noise to all experiments to acquire noisy observation data. To assess the noise immunity of our method, we conducted a comprehensive noise immunity test, focusing on the Marmousi-2 model extracted from SEG/EAGE, and performed a comparative analysis involving multiple methodologies. The remaining parameters remained consistent with those used in the previous segment. Initially, we executed a series of noise tests on the inverted seismic data, with the signal-to-noise ratio set at 5 dB. The outcomes are depicted in Fig. 11 below, indicating a substantial impact of noise on the seismic records.

Fig. 12 presents the inversion results and partial enlargements obtained from four methods. Fig. 12(a)—(d) illustrate the inverted velocity profiles using regular FWI without any regularization, TV-FWI, ATpV-FWI and FATpV-FWI, respectively. Correspondingly, Fig. 12(e)—(h) depict the partially enlarged views. Notably, at a signal-to-noise ratio of 5 dB, all four methods demonstrate

 Table 1

 The three indexes (SSIM/PSNR/RMSE) of the modification Marmousi model.

Method	SSIM	PSNR	RMSE
FWI	0.3300	23.2968	304.4533
TV-FWI	0.4377	23.6738	294.8860
ATpV-FWI	0.4452	23.6643	292.5311
FATpV-FWI	0.4839	23.7065	290.4251

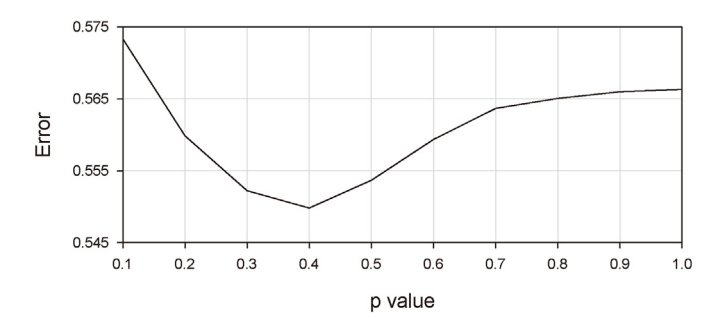


Fig. 14. p-value error analysis.

commendable reconstruction results in the upper segment of the Marmousi velocity model and the low-velocity area. However, the efficacy of FWI without any regularization and FWI with conventional TV remains constrained, particularly in deeper layers, where the information recovery and inversion results are less satisfactory. In contrast, the FWI with FATpV method exhibits significant

enhancements in velocity size and edge delineation, particularly in deeper regions of the model. It excels in accurately reconstructing smooth transitions and sharpened interfaces. As indicated by the arrow in the figure, the FWI with FATpV method demonstrates superior effectiveness. To facilitate a more precise comparison of the inversion outcomes, we extracted single-channel data for analysis.

Fig. 13 shows a single channel comparison of the inversion results in Fig. 12, where light green represents the initial velocity, black represents the theoretical velocity, sky blue represents the conventional inversion result, blue represents the TV-FWI inversion result, magenta represents the ATpV-FWI inversion result, and red represents the method proposed in this paper. From the graph, it can be seen that the red color has the best effect. Additionally, we quantitatively evaluated the performance of the three inversion methods using normalized model root mean square error (RMSE), peak signal-to-noise ratio (PSNR), and structural similarity index (SSIM), as demonstrated in Table 1 These metrics further substantiate the efficacy of the FATpV method.

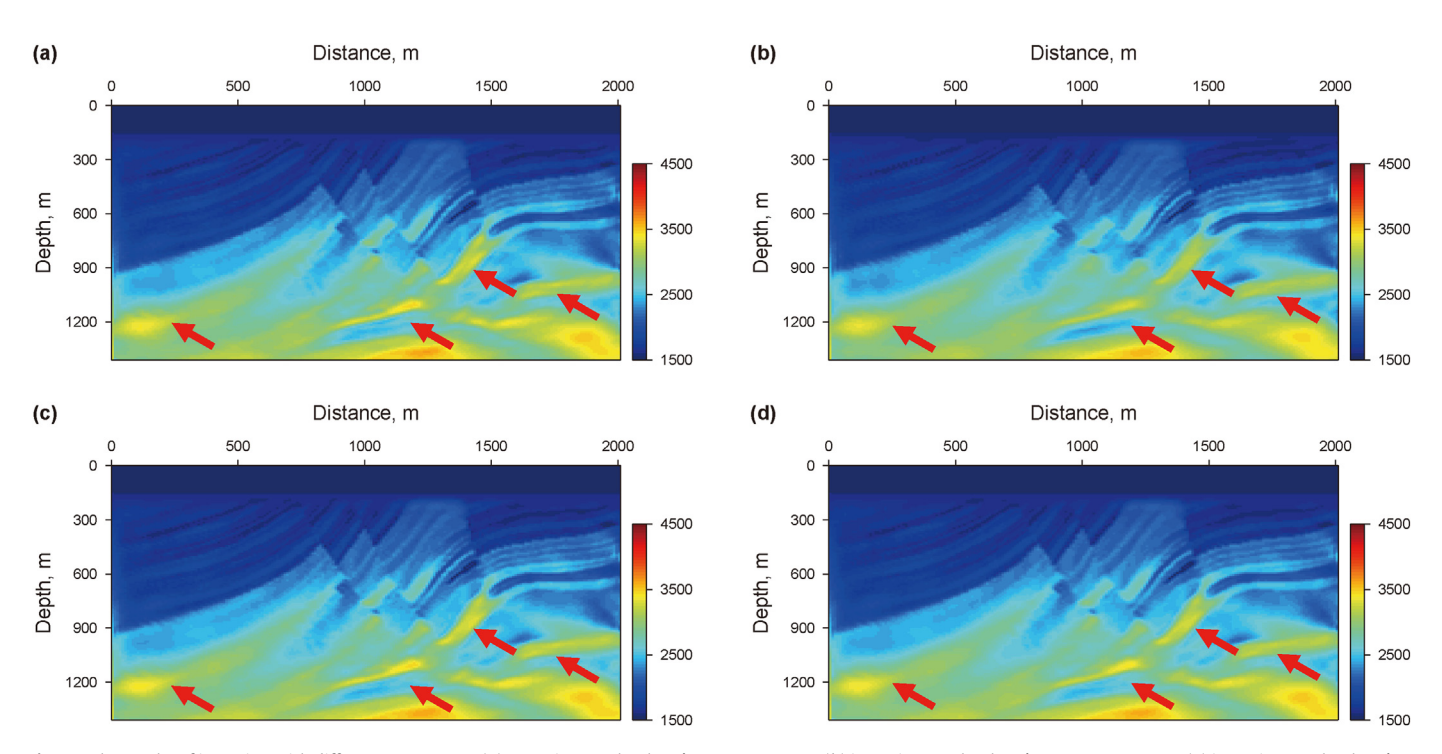


Fig. 15. The results of inversion with different parameters. **(a)** Inversion result when $\lambda = 0.08$, $\eta = 0.1$; **(b)** inversion result when $\lambda = 0.08$, $\eta = 0.001$; **(c)** inversion result when $\lambda = 0.08$, $\eta = 0.01$; **(d)** inversion result when $\lambda = 0.001$, $\eta = 0.01$.

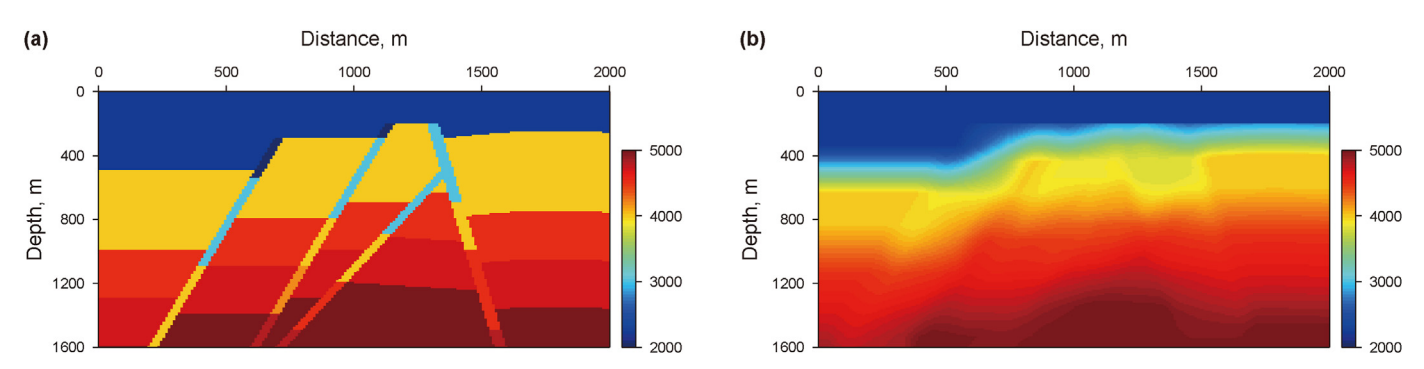


Fig. 16. The theoretical model. (a) Velocity model; (b) initial velocity model.

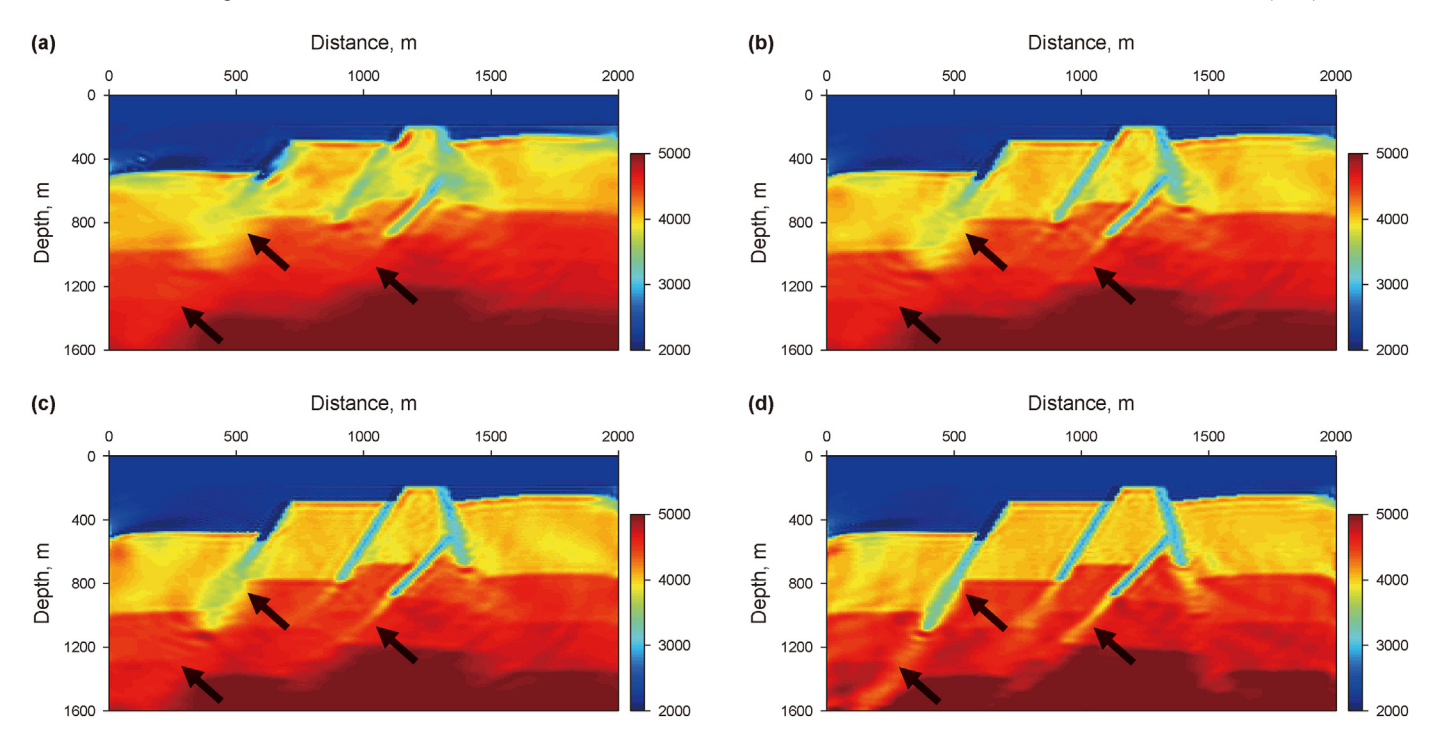


Fig. 17. FWI example: inverted velocity using (a) regular FWI without any regularization, (b)TV-FWI, (c) ATpV-FWI, and (d) FATpV-FWI.

In order to analyze the selection range of fractional order p-values, we conducted statistical analysis on the Marmousi model. Fig. 14 illustrates the error analysis conducted on the selection of p-value during the inversion process. In this experiment, the error value is minimized when the p-value is set to 0.4. When conducting the inversion, it is typically recommended to choose p-values between 0.2 and 0.5 for optimal results based on experience.

We compared the impact of the values of $\hat{\lambda}$ and η on the inversion results, as illustrated in Fig. 15. Fig. 15(a), (b) depict the inversion results when η is set to 0.1 and 0.0001, respectively. It can be observed from the figures that when η is set to an excessively large or small value, the inversion results are affected, resulting in low resolution. Similarly, Fig. 15(c), (d) show the inversion results when λ is set to 0.1 and 0.0001, respectively. When the value of λ is inaccurately selected, it also affects the resolution of the inversion results, as indicated by the red arrows in the figures. In this paper, λ is set to 0.08, and η is set to 0.01. Typically, the range of λ is between 0.01 and 0.1, while η ranges from 0.001 to 0.01. However, the specific values need to be adjusted based on the inversion results.

This model is based on geological features from Brady's Enhanced Geothermal System (EGS) site in Nevada, USA. It includes several steeply dipping fault zones, with widths much smaller than the seismic wavelengths. The maximum dip angle of these fault zones is approximately 82°. Due to the presence of small intermediate fractures, the model presents challenges for migration and inversion. Fig. 16(a) shows the theoretical velocity model, while Fig. 16(b) presents the initial velocity model. The model consists of grid points configured as $nx \times nz = 200 \times 160$, with a grid spacing of $\Delta x = \Delta z = 10$ m, a time step of $\Delta t = 1$ ms, and a total of 20 shots recorded over 1.8 s. The seismic source used is a 20 Hz Ricker wavelet, with detectors uniformly distributed across the surface.

Fig. 17 presents the inversion results from four methods. As shown in the figure, the regular FWI and TV regularized inversion results generally capture the overall structural features of the model. In particular, when the layers are relatively homogeneous and the wavefield variation is smooth, the inversion results

accurately reflect large-scale structural characteristics. However, due to the influence of small faults in the subsurface, the waveforms become more complex. Small faults, with scales smaller than the seismic wavelength, lead to increased local complexity in the wavefield. This complexity is especially pronounced under the effects of multiple reflections or diffraction waves, making the waveform more intricate. Both the traditional FWI method and TV regularization struggle to accurately capture such local complexities, limiting the effectiveness of the inversion methods. In contrast, the FATpV-FWI method offers higher accuracy by

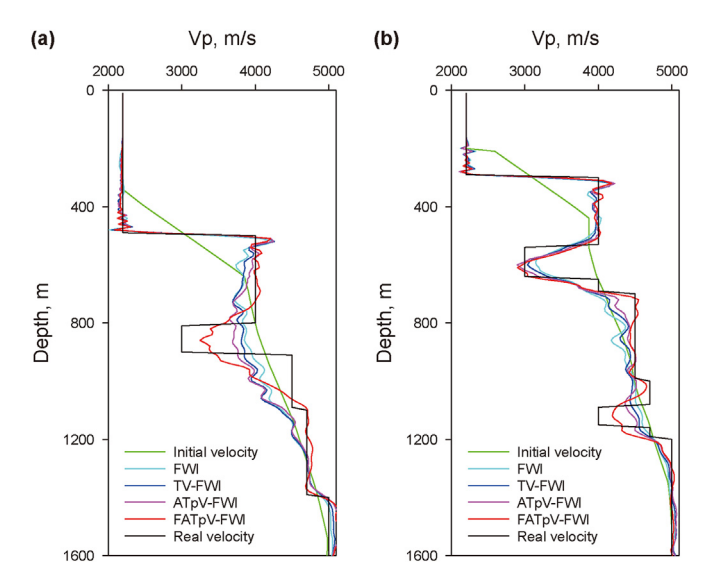


Fig. 18. FWI example: comparison of different velocities at two locations. Velocity comparison at (a) x = 500 m, (b) x = 1500 m. (Light green represents the initial velocity, black represents the theoretical velocity, sky blue represents the conventional inversion result, blue represents the TV-FWI inversion result, magenta represents the ATpV-FWI inversion result, and red represents the FATpV-FWI inversion result.)

Table 2Comparison of computational time for the models in the paper.

Method	FWI	TV-FWI	ATpV-FWI	FATpV-FWI
BG Compass model	9.46 h	9.56 h	10.44 h	10.51 h
Marmousi model	5.25 h	5.43 h	5.74 h	5.77 h

constructing sparse inversion constraints, which provide additional restrictions and improve the inversion results, particularly in the presence of small-scale faults and deep parameters. Fig. 18 shows a single-channel comparison of the four methods. From the figure, it is evident that the FATpV-FWI inversion achieves the best results, closely matching the theoretical model. The calculation time of the model in this paper is shown in Table 2.

4. Conclusion

In this paper, we introduce a fractional-order anisotropic total variation FWI method based on L_p quasi-norm. Extending beyond the traditional integer-order difference, this approach incorporates fractional-order differences, mitigating the effects associated with integer-order differences and reducing scattering effects, thereby enhancing inversion accuracy. The results obtained from the BG Compass model demonstrate superior performance in deep seismic parameter inversion compared to traditional FWI methods. Moreover, the application to the Marmousi model showcases the method's capability to capture more detailed information, further improving inversion accuracy. In the future, we will extend the method to three-dimensional full waveform inversion, which offers a promising direction for further advancements. However, this expansion introduces significant challenges, particularly in terms of computational efficiency and time consumption. The increased complexity of 3D models will require more advanced computational resources, potentially leading to longer inversion times. To overcome this, future work will focus on optimizing computational efficiency through strategies such as parallel processing and more efficient numerical algorithms, making 3D FWI viable for largescale reservoir modeling applications. Furthermore, incorporating anisotropic models and refining regularization techniques will be essential to enhancing the method's stability and accuracy in more complex environments.

CRediT authorship contribution statement

Bo Li: Writing — review & editing, Writing — original draft, Funding acquisition, Formal analysis, Data curation, Conceptualization. **Xiao-Tao Wen:** Conceptualization. **Yu-Qiang Zhang:** Investigation. **Zi-Yu Qin:** Data curation. **Zhi-Di An:** Software.

Conflict of interest statement

We declare that we have no financial and personal relationships with other people or organizations that can inappropriately influence our work, there is no professional or other personal interest of any nature or kind in any product, service and/or company that could be construed as influencing the position presented in, or the review of, the manuscript entitled.

Acknowledgments

This work was supported by the China Postdoctoral Science Foundation (Grant No.2024MF750281), the Postdoctoral Fellowship Program of CPSF (Grant No. GZC20230326), the Natural Science Foundation Project of Sichuan Province (Grant

No.2025ZNSFSC1170) and Sichuan Science and Technology Program (Grant No.2023ZYD0158). The authors who contributed to the writing and revision of this article are greatly appreciated. The authors thank the editorial board and the reviewers for their valuable and constructive suggestions.

Appendix A

Eq. (8) above is expressed as:

$$\begin{cases} \mathbf{m}_{l+1} = \min_{\mathbf{m}} \left\{ \frac{1}{2} \|\mathbf{d}_{obs} - \mathbf{d}_{cal}(\mathbf{m})\|_{2}^{2} + \frac{\eta}{2} \|\mathbf{m} - \mathbf{w}_{l} + \mathbf{b}_{l}\|_{2}^{2} \right\} \\ \mathbf{w}_{l+1} = \min_{\mathbf{w}} \left\{ \lambda \left(\|\mathbf{m} \mathbf{D}_{x}^{a}\|_{p}^{p} + \left\| \mathbf{D}_{y}^{a} \mathbf{m} \right\|_{p}^{p} \right) + \frac{\eta}{2} \|\mathbf{m}_{l+1} - \mathbf{w} + \mathbf{b}_{l}\|_{2}^{2} \right\} \\ \mathbf{b}_{l+1} = \mathbf{b}_{l} + \mathbf{m}_{l+1} - \mathbf{w}_{l+1} \end{cases}$$
(A1)

For this equation, we use the ADMM algorithm to perform a step-by-step iterative solution, updating \mathbf{m}_{l+1} , \mathbf{w}_{l+1} and \mathbf{b}_{l+1} respectively. For the update of \mathbf{m}_{l+1} , we can use the gradient algorithm to solve it. Here, we derive the update process of \mathbf{w}_{l+1} . We can choose to use split-Bregman iteration technique or continue to use ADMM for updating. The ADMM algorithm updates can be reformulated in the following form:

$$J = \operatorname{argmin}\left\{\frac{\eta}{2}\|\mathbf{m}_{l+1} - \mathbf{w} + \mathbf{b}_{l}\|_{2}^{2} + \lambda \left(\|\mathbf{m}\mathbf{D}_{x}^{a}\|_{p}^{p} + \|\mathbf{D}_{y}^{a}\mathbf{m}\|_{p}^{p}\right)\right\},$$
(A2)

Then introduce the Lagrange multiplier term L_x and L_y :

$$J = \operatorname{argmin} \left\{ \|\mathbf{m}_{l+1} - \mathbf{w} + \mathbf{b}_l\|_2^2 + \frac{2\lambda}{\eta} \left(\|\mathbf{L}_X\|_p^p + \|\mathbf{L}_y\|_p^p \right) \right\}$$

s.t $\mathbf{L}_X = \mathbf{m} \mathbf{D}_X^a, \mathbf{L}_y = \mathbf{D}_y^a \mathbf{m},$ (A3)

In the above equation, we assume $\xi = \frac{2\lambda}{\eta}$, introducing dual terms C_X and C_Y , and the above equation becomes an unconstrained problem:

$$J = \operatorname{argmin} \left\{ \|\mathbf{m}_{l+1} - \mathbf{w} + \mathbf{b}_{l}\|_{2}^{2} + \xi \left(\|\mathbf{L}_{x}\|_{p}^{p} + \|\mathbf{L}_{y}\|_{p}^{p} \right) + \nu \|\mathbf{L}_{x} - \mathbf{m}\mathbf{D}_{x}^{a} - \mathbf{C}_{x}\|_{2}^{2} + \nu \|\mathbf{L}_{y} - \mathbf{D}_{y}^{a}\mathbf{m} - \mathbf{C}_{y}\|_{2}^{2} \right\},$$
(A4)

The variables in the above equation can be extracted and their subfunctions about ${\bf m}$ can be:

$$J = \operatorname{argmin} \left\{ \|\mathbf{m}_{l+1} - \mathbf{w} + \mathbf{b}_{l}\|_{2}^{2} + \nu \|\mathbf{L}_{x} - \mathbf{m}\mathbf{D}_{x}^{a} - \mathbf{C}_{x}\|_{2}^{2} + \nu \|\mathbf{L}_{y} - \mathbf{D}_{y}^{a}\mathbf{m} - \mathbf{C}_{y}\|_{2}^{2} \right\},$$
(A5)

Derive this equation and make the derivative equal to 0, then you can get \mathbf{m} . Then extract the variables from Eq. (A4) and let them be subfunctions about \mathbf{L}_{x} and \mathbf{L}_{y} , which can be expressed as:

$$J = \operatorname{argmin} \left\{ \xi \| \boldsymbol{L}_{x} \|_{p}^{p} + \nu \| \boldsymbol{L}_{x} - \boldsymbol{m} \boldsymbol{D}_{x}^{a} - \boldsymbol{C}_{x} \|_{2}^{2} \right\}, \tag{A6}$$

$$J = \operatorname{argmin}\left\{\xi \|\mathbf{L}_y\|_p^p + \nu \|\mathbf{L}_y - \mathbf{D}_y^a \mathbf{m} - \mathbf{C}_y\|_2^2\right\},\tag{A7}$$

For Eqs. (A6) and (A7), the soft threshold shrinkage algorithm can be used to solve and update, respectively expressed as:

$$L_{x}^{i+1} = \max\left(\left|\mathbf{m}\mathbf{D}_{x}^{a} + \mathbf{C}_{x}\right| - (\nu/\xi)^{p-2} \cdot \left|\mathbf{m}\mathbf{D}_{x}^{a} + \mathbf{C}_{x}\right|^{p-1}, 0\right) \cdot \operatorname{sign}(\mathbf{m}\mathbf{D}_{x}^{a} + \mathbf{C}_{x}), \tag{A8}$$

$$\mathbf{L}_{y}^{i+1} = \max\left(\left|\mathbf{D}_{y}^{a}\mathbf{m} + \mathbf{C}_{y}\right| - (\nu/\xi)^{p-2} \cdot \left|\mathbf{D}_{y}^{a}\mathbf{m} + \mathbf{C}_{y}\right|^{p-1}, 0\right) \cdot \operatorname{sign}\left(\mathbf{D}_{v}^{a}\mathbf{m} + \mathbf{C}_{v}\right), \tag{A9}$$

Further bring the above results into the sub-functions of C_x and C_y :

$$J\left(\boldsymbol{C}_{x}^{i+1}\right) = \min \nu \left\|\boldsymbol{L}_{x} - \mathbf{m}\boldsymbol{D}_{x}^{a} - \boldsymbol{C}_{x}\right\|_{2}^{2},\tag{A10}$$

$$J(\boldsymbol{C}_{y}^{i+1}) = \min \nu \left\| \boldsymbol{L}_{y} - \boldsymbol{\mathbf{D}}_{y}^{a} \boldsymbol{\mathbf{m}} - \boldsymbol{C}_{y} \right\|_{2}^{2}, \tag{A11}$$

This type of function is mainly a convex optimization function, and its gradient is directly obtained for updating. The update equation can be expressed as:

$$\mathbf{C}_{\mathbf{X}}^{i+1} = \mathbf{C}_{\mathbf{X}}^{i} + \mathbf{m}\mathbf{D}_{\mathbf{X}}^{a} - \mathbf{L}_{\mathbf{X}},\tag{A12}$$

$$\boldsymbol{C}_{v}^{i+1} = \boldsymbol{C}_{v}^{i} + \mathbf{D}_{v}^{a} \mathbf{m} - \boldsymbol{L}_{y}, \tag{A13}$$

Finally, after updating \mathbf{m}_{l+1} and \mathbf{w}_{l+1} , you can update \mathbf{b}_{l+1} .

References

- Aghamiry, H.S., Gholami, A., Operto, S., 2019a. ADMM-based multiparameter wavefield reconstruction inversion in VTI acoustic media with TV regularization. Geophys. J. Int. 219 (2), 1316–1333. https://doi.org/10.1093/gji/ggz369.
- Aghamiry, H.S., Gholami, A., Operto, S., 2019b. Compound regularization of full-waveform inversion for imaging piecewise media. IEEE Trans. Geosci. Rem. Sens. 58 (2), 1192–1204. https://doi.org/10.1109/TGRS.2019.2944464.
- Aghamiry, H.S., Gholami, A., Operto, S., 2018. Hybrid Tikhonov+ total-variation regularization for imaging large-contrast media by full-waveform inversion. In: SEG Int. Expo. Annu. Meet. https://doi.org/10.1190/segam2018-2996968.1. SEG_SEG_2018-2996968.
- Bai, J., Feng, X., 2007. Fractional-order anisotropic diffusion for image denoising. IEEE Trans. Image Process. 16 (10), 2492–2502. https://doi.org/10.1109/ TIP 2007 904971
- Barnier, G., Biondi, E., Clapp, R.G., et al., 2023. Full-waveform inversion by model extension: theory, design, and optimization. Geophysics 88 (5), R579–R607. https://doi.org/10.1190/geo2022-0350.1.
- Boyd, S., Parikh, N., Chu, E., et al., 2011. Distributed optimization and statistical learning via the alternating direction method of multipliers. Found. Trends Mach. Learn. 3 (1), 1–122. https://doi.org/10.1561/2200000016.
- Brossier, R., Operto, S., Virieux, J., 2009. Robust elastic frequency-domain full-waveform inversion using the L₁ norm. Geophys. Res. Lett. 36 (20). https://doi.org/10.1029/2009GI.039458.
- Brossier, R., Operto, S., Virieux, J., 2010. Which data residual norm for robust elastic frequency-domain full waveform inversion? Geophysics 75 (3), R37–R46. https://doi.org/10.1190/1.3379323.
- Burstedde, C., Ghattas, O., 2009. Algorithmic strategies for full waveform inversion:

 1D experiments. Geophysics 74 (6), WCC37–WCC46. https://doi.org/10.1190/
- Chen, H., Gao, J., Zhang, B., 2020. An adaptive time-varying seismic super-resolution inversion based on L_p regularization. Geosci. Rem. Sens. Lett. IEEE 18 (8), 1481-1485. https://doi.org/10.1109/LGRS.2020.3000339.
- Didas, S., Burgeth, B., Imiya, A., et al., 2005. Regularity and scale-space properties of fractional high order linear filtering. In: Scale Space and PDE Methods in Computer Vision: 5th International Conference, Scale-Space 2005, Hofgeismar, Germany, April 7–9, 2005. Proceedings 5. Springer Berlin Heidelberg, pp. 13–25. https://doi.org/10.1007/11408031_2.
- Esser, E., Guasch, L., van Leeuwen, T., et al., 2018. Total variation regularization strategies in full-waveform inversion. SIAM J. Imag. Sci. 11 (1), 376–406. https://doi.org/10.1137/17M111328X.
- Guitton, A., 2012. Blocky regularization schemes for full-waveform inversion. Geophys. Prospect. 60 (5), 870–884. https://doi.org/10.1111/j.1365-2478.2012.01025.x.

- Guo, Y.D., Huang, J.P., Chao, C., et al., 2020. Sparse constrained encoding multi-source full waveform inversion method based on K-SVD dictionary learning. Appl. Geophys. 17 (1), 111–123. https://doi.org/10.1007/s11770-019-0797-7.
- Gupta, H., Fageot, J., Unser, M., 2018. Continuous-domain solutions of linear inverse problems with Tikhonov versus generalized TV regularization. IEEE Trans. Signal Process. 66 (17), 4670–4684. https://doi.org/10.1109/TSP.2018.2860549.
- Kalita, M., Kazei, V., Choi, Y., et al., 2019. Regularized full-waveform inversion with automated salt flooding. Geophysics 84 (4), R569–R582. https://doi.org/ 10.1190/geo2018-0146.1.
- Lin, Y., Huang, L., 2014. Acoustic-and elastic-waveform inversion using a modified total-variation regularization scheme. Geophys. J. Int. 200 (1), 489–502. https://doi.org/10.1093/gii/ggu393.
- Li, Z., Qu, Y., 2022. Research progress on seismic imaging technology. Pet. Sci. 19 (1), 128–146. https://doi.org/10.1016/i.petsci.2022.01.015.
- Li, J., Zhu, J., Qu, Y., et al., 2024. Elastic full-waveform inversion based on the double-cross-shaped discrete flux-corrected transport. Geophys. Prospect. 72 (2), 468–483. https://doi.org/10.1111/1365-2478.13420.
- Li, J., Zhu, J., Qu, Y., et al., 2023. Seismic full-waveform inversion based on super-resolution for high-precision prediction of reservoir parameters. Geophysics 88 (3), R243–R256. https://doi.org/10.1190/geo2022-0006.1.
- Li, S., He, Y., Chen, Y., et al., 2018a. Fast multi-trace impedance inversion using anisotropic total p-variation regularization in the frequency domain. J. Geophys. Eng. 15 (5), 2171–2182. https://doi.org/10.1088/1742-2140/aaca4a.
- Li, S., Peng, Z., Wu, H., 2018b. Prestack multi-gather simultaneous inversion of elastic parameters using multiple regularization constraints. J. Earth Sci. 29, 1359–1371. https://doi.org/10.1007/s12583-017-0905-7.
- Li, X., Esser, E., Herrmann, F.J., 2016. Modified Gauss-Newton full-waveform inversion explained—why sparsity-promoting updates do matter. Geophysics 81 (3), R125—R138. https://doi.org/10.1190/geo2015-0266.1.
- Mora, P., 1987. Nonlinear two-dimensional elastic inversion of multioffset seismic data. Geophysics 52 (9), 1211–1228. https://doi.org/10.1190/1.1442384.
- Plessix, R.E., 2006. A review of the adjoint-state method for computing the gradient of a functional with geophysical applications. Geophys. J. Int. 167 (2), 495–503. https://doi.org/10.1111/j.1365-246X.2006.02978.x.
- Plessix, R.E., 2009. Three-dimensional frequency-domain full-waveform inversion with an iterative solver. Geophysics 74 (6), WCC149–WCC157. https://doi.org/10.1190/1.3211198.
- Qu, S., Verschuur, E., Chen, Y., 2019. Full-waveform inversion and joint migration inversion with an automatic directional total variation constraint. Geophysics 84 (2), R175–R183. https://doi.org/10.1190/geo2018-0085.1.
- Qu, Y., Guan, Z., Li, J., Li, Z., et al., 2020. Fluid-solid coupled full-waveform inversion in the curvilinear coordinates for ocean-bottom cable data. Geophysics 85 (3), R113—R133. https://doi.org/10.1190/geo2018-0743.1.
- Tarantola, A., 1984. Inversion of seismic reflection data in the acoustic approximation. Geophysics 49 (8), 1259–1266. https://doi.org/10.1190/1.1441754.
- Virieux, J., Operto, S., 2009. An overview of full-waveform inversion in exploration geophysics. Geophysics 74 (6), WCC1–WCC26. https://doi.org/10.1190/
- Warner, M., Guasch, L., 2016. Adaptive waveform inversion: theory. Geophysics 81 (6), R429–R445. https://doi.org/10.1190/geo2015-0387.1.
- Woodworth, J., Chartrand, R., 2016. Compressed sensing recovery via nonconvex shrinkage penalties. Inverse Probl. 32 (7), 075004. https://doi.org/10.1088/0266-5611/32/7/075004.
- Wu, H., He, Y., Chen, Y., et al., 2019. Seismic acoustic impedance inversion using mixed second-order fractional ATpV regularization. IEEE Access 8, 3442–3452. https://doi.org/10.1109/ACCESS.2019.2962552.
- Xue, Z., Zhu, H., Fomel, S., 2017. Full-waveform inversion using seislet regularization. Geophysics 82 (5), A43–A49. https://doi.org/10.1190/geo2016-0699.1.
- Yao, G., Wu, D., Wang, S., 2020. A review on reflection-waveform inversion. Pet. Sci. 17, 334–351. https://doi.org/10.1007/s12182-020-00431-3.
- Yong, P., Liao, W., Huang, J., 2018. Total variation regularization for seismic waveform inversion using an adaptive primal dual hybrid gradient method. Inverse Probl. 34 (4), 045006. https://doi.org/10.1088/1361-6420/aaaf8e.
- Yu, C., Wang, Y., Zhao, J., et al., 2014. Double parameterized regularization inversion method for migration velocity analysis in transversely isotropic media with a vertical symmetry axis. Geophys. Prospect. 62 (5), 1040–1053. https://doi.org/ 10.1111/1365-2478.12117
- Zhang, S., Huang, J., Wang, Z., 2022. Wavefield reconstruction inversion with weak-total-variation constraint based on first arrival traveltime tomography. Appl. Geophys. 19 (2), 232–243. https://doi.org/10.1007/s11770-022-0941-7.
- Zhang, Y., Pu, Y.F., Hu, J.R., et al., 2012. A class of fractional-order variational image inpainting models. Appl. Math. Inf. Sci. 6 (2), 299–306.
- Zhu, L., Liu, E., McClellan, J.H., 2017. Sparse-promoting full-waveform inversion based on online orthonormal dictionary learning. Geophysics 82 (2), R87–R107. https://doi.org/10.1190/geo2015-0632.1.
- Zhu, W., Xu, K., Darve, E., et al., 2022. Integrating deep neural networks with full-waveform inversion: reparameterization, regularization, and uncertainty quantification. Geophysics 87 (1), R93–R109. https://doi.org/10.1190/geo2020-0933.1.